Available online at www.sciencedirect.com
ScienceDirect
Journal of Power Sources 178 (2008) 258–268
JOURNAL OF POWER SOURCES
www.elsevier.com/locate/jpowsour

Two-phase flow and evaporation in model fibrous media Application to the gas diffusion layer of PEM fuel cells

O. Chapuis, M. Prat *, M. Quintard, E. Chane-Kane, O. Guillot, N. Mayer

Institut de Mécanique des Fluides de Toulouse, UMR CNRS-INP/UPS No. 5502, Avenue du Professeur Camille Soula, 31400 Toulouse, France

Received 10 July 2007; received in revised form 26 November 2007; accepted 1 December 2007
Available online 14 December 2007

Abstract

Two-phase flow dominated by capillary effects in model fibrous media is studied combining pore-network simulations and visualisations on transparent micromodels. It is shown that the process of liquid water invasion in a hydrophobic medium can be simulated using the classical invasion percolation algorithm provided that the contact angle (measured in air, which is the wetting phase) is sufficiently far below 90°. For contact angles approaching 90°, changes in the interface local growth mechanisms lead to changes in the invasion pattern.

Then it is shown that the invasion pattern is dramatically different in a hydrophilic medium. Impact of wettability (hydrophobic vs. hydrophilic) on evaporation pattern is also analysed.

In a last part, implications of the study findings on the water management problem in the gas diffusion layers (GDLs) of PEMFC are discussed. Our results provide pore-scale explanations to the advantages of hydrophobic GDLs.

Keywords: PEM fuel cell; Gas diffusion layer; Two-phase flow; Evaporation; Wettability; Porous media

1. Introduction

PEM fuel cells are undergoing intense development. Many groups work throughout the world in order to improve their performances, efficiency, reliability, manufacturability and cost-effectiveness. In this context, one popular way for studying fuel cells is to develop computational models representing the complex multi-physics transport processes occurring in fuel cells. This leads to rather complex coupled models taking into account the fluidic, ionic, electronic and thermal transports in concert with electrochemical reactions, e.g. Refs. [1–4] and references therein.

While much progress has been made in recent years, the development of truly predictive models remains a challenge due to fundamental modelling issues. Among the identified issues, see for instance the discussion in Ref. [5], one of the major concerns is the modelling, and, more generally, the understanding, of two-phase flow in the gas diffusion layer (GDL).

The GDLs consist of an anisotropic fibrous structure, either in the form of a random structure (carbon paper) or woven carbon fabrics or cloths. The thickness of a GDL typically varies between 170 and 400 μm [6], whereas the fibre diameter is typically of the order of 10 μm (carbon-paper GDL) leading to a distribution of pore sizes ranging from a few microns to tens of microns [7]. The overall porosity of a GDL is in the range 70–80%. Thus a GDL appears as a highly anisotropic fibrous structure very thin in the main direction of transport with thickness of only a few tens of fibre diameters. Depending on the applications considered, one or several microporous layers (MPLs) may be attached to the fibrous structure [6], in order to improve the electrical contact with the catalyst layer (CL) and the control of the water management. However, the microstructure of the MPL is quite different from that of the macro-porous substrate described above and the specific effect of the MPL is not studied in this paper.

The GDL are commonly teflonized, rendering them hydrophobic. The degree of hydrophobicity is a priori dependent upon the amount of Teflon added to the GDL. A classic

* Corresponding author at: Institut de Mécanique des Fluides de Toulouse, UMR CNRS-INP/UPS No. 5502, GEMP, Avenue du Professeur Camille Soula, 31400 Toulouse, France. Tel.: +33 561285883; fax: +33 561285899.
E-mail address: prat@imft.fr (M. Prat).

0378-7753/$ – see front matter © 2007 Elsevier B.V. All rights reserved.
doi:10.1016/j.jpowsour.2007.12.011

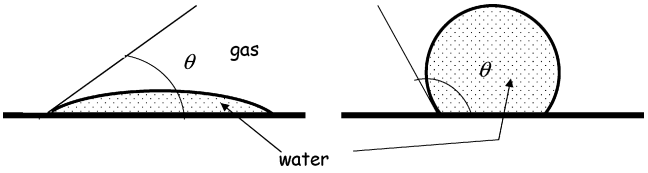

Fig. 1. Hydrophilic ($\theta < \pi/2$) and hydrophobic ($\theta > \pi/2$) surfaces.

way of characterizing the hydrophobicity is to use the concept of contact angle, which is the angle θ between the solid phase and the interface between the two fluids (see Fig. 1). When the two fluids are liquid water and air, the surface is said to be hydrophilic when this angle measured in the water is lower than 90° and hydrophobic when $\theta > 90°$. The contact angle for water on a Teflon flat surface is roughly 110°, whereas water on a carbon surface is close to 80° (thus hydrophilic). The measurement of contact angle using the sessile drop method on a teflonized GDL carbon cloth is reported in Ref. [8]. It is found to be 133°. The increased contact angle as compared to a flat surface is attributed to the surface roughness of the GDL. The contact angle is generally measured at room temperature. Variations of contact angle with temperature are a priori expected. It would be therefore interesting to measure it at temperatures representative of PEM fuel cell operating conditions (∼80 °C). While a major change in wettability (i.e., from hydrophobicity to hydrophilicity) is not expected, it would be interesting to evaluate the influence of varying contact angles. Another issue is that the contact angle exhibits hysteresis, meaning that the advancing (θ_a) and receding (θ_r) contact angles may be very different, with the advancing contact angle being typically greater than the receding one. The difference is on the order of 14° for distilled water on a Teflon flat surface according to the measurements reported in Ref. [8] (with $\theta_a \approx 127°$ and $\theta_r \approx 113°$). As pointed out in Ref. [9], measurements of contact angle on a pure Teflon flat plate or at the external surface of a GDL are, however, not necessarily representative of the internal contact angle, i.e. the average contact angle within the pore space of a GDL. The values of the internal contact angle in GDL materials reported in Ref. [9] are in the range [88°, 101°], depending on the GDL materials considered and therefore significantly lower than the expected value on a pure Teflon plate. As we shall see, the wettability (i.e., the hydrophobic or hydrophilic nature) of the GDL has a great impact on the water transport, especially in the range of contact angles close to 90°. The motivation for rendering the GDL hydrophobic is generally associated with the idea that the hydrophobicity will limit the flooding of the GDL, for example by forcing the water to agglomerate at the free surface of the GDL [5]. The results presented in this paper will shed some light on these different aspects.

Another important issue is the general validity of macroscale two-phase flow models commonly used when modelling transport phenomena in GDLs and/or between the GDL and the catalyst layer, e.g. Ref. [10]. Generally, these models are the conventional models developed for studying flow in "usual" porous media, such as soils or sedimentary rocks. They are based on the so-called generalized Darcy's law and the concepts of macroscopic capillary pressure and relative permeability, see for instance Ref. [11]. In principle, this type of model is intimately related to the concept of representative elementary volume (REV), e.g. Ref. [12]. This volume is supposed to be large enough for being representative of the microstructure but also sufficiently small compared to the porous domain size. As mentioned before, the thickness of a GDL is typically on the order of a few tens of fibre or pore sizes, which is presumably on the order or less than the REV size. This raises fundamental questions regarding the meaning to be given to the fields, such as saturation, pressures and velocities, computed across the GDL using this type of model. Hence, using this type of modelling is not only difficult because of the lack of data for the various fibrous materials forming a GDL, as pointed out for example in Ref. [5], but raises also a more fundamental question regarding the validity of the continuum approach applied to ultra-thin porous media such as the GDL.

The fact that this approach has not yet been validated at all for the GDLs is a well-identified problem, e.g. Refs. [4,5,7]. Hence, there is a need for a better understanding of two-phase flows in GDLs, in particular from a micro-scale perspective. In this respect, visualisations of liquid water in a GDL and of its evolution are certainly useful. Although in situ visualisations, e.g. Ref. [13], are certainly the best option to truly understand the physics of two-phase flows in GDLs of PEMFC, ex situ visualisations, e.g. Ref. [14], are also useful for improving our understanding of two-phase flows and providing data for comparison with models. On the modelling side, one option is to develop simulations directly at the scale of the microstructure, see for example Ref. [15]. In addition to a better understanding of the physics, this type of simulation can be useful for evaluating the validity of the traditional continuum approach and also for computing data difficult to measure in very thin systems, such as the capillary pressure–saturation curve or the relative permeabilities. In this context, although limited to 2D model porous media, the results presented in this paper can be seen as a contribution to a better understanding of two-phase flow in model fibrous media in relation with the general problems of two-phase flow modelling in GDLs and the impact of wettability mentioned above.

The paper is organized as follows: first we present in Section 2 a model of liquid water quasi-static invasion in a hydrophobic model fibrous medium. Results of simulation are compared to experimental visualisations. In Section 3, we concentrate on the influence of contact angle on the invasion pattern. In Section 4, we recall recent results regarding the impact of wettability on evaporation patterns. Impacts of the results on two-phase flows in GDLs are discussed in Section 5.

2. Quasi-static invasion of liquid water in a model 2D fibrous medium

As a matter of fact, how water flooding occurs in a GDL is not perfectly clear. For example, Nam and Kaviany [16], tend to consider that liquid water invades the GDL as a result of a condensation process. In other studies, e.g. Ref. [17], the condensation process is not taken into account and water enters directly as a liquid phase into the GDL from the CL/GDL interface. The invasion in liquid phase from one face of the fibrous material

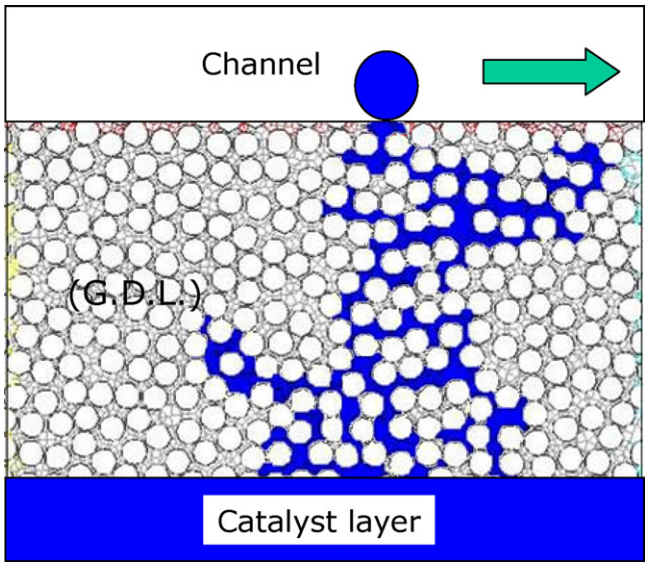

Fig. 2. Invasion scenario. Liquid water invades the GDL from the catalyst layer.

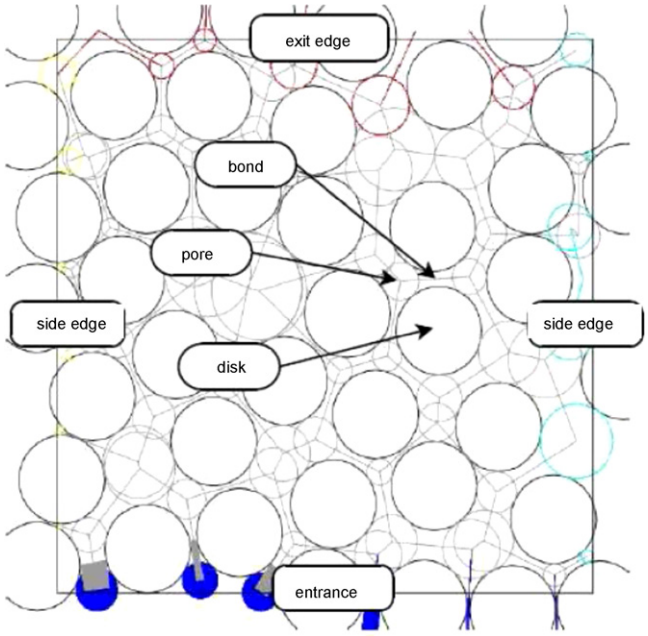

Fig. 3. Model fibrous medium, Voronoi diagram and pore network.

is also the situation considered in the pore-scale simulations of Schulz et al. [15], and the visualisation experiment presented in Ref. [14]. Although the condensation process and liquid phase invasion from the CL are likely to occur simultaneously in an operating fuel cell, we consider in this paper the same invasion scenario as in Refs. [14] or [17] and therefore suppose that liquid water enters the fibrous domain from one side. This situation is sketched in Fig. 2. Whatever the exact scenario in an operating fuel cell, this situation is interesting, in any case, for evaluating two-phase flow models. Initially, the fibrous material is dry with air occupying the pore space. Then liquid water is injected into the pore space from one side of the porous domain until breakthrough, i.e. until water reaches the side opposite to the injection side (which corresponds to the bipolar plate channel in a PEMFC).

In this section, we assume that the GDL is hydrophobic. Hence liquid water is the non-wetting fluid and air the wetting one. The process of immiscible displacement of a wetting fluid by a non-wetting one is usually called drainage, e.g. Ref. [11]. Therefore the invasion of liquid water into a dry hydrophobic fibrous material corresponds to a drainage process. This process was studied in detail in Ref. [18]. As shown in Ref. [18], this process is controlled by the competition between capillary effects and viscous effects (assuming negligible gravity effects). The invasion pattern depends on two parameters: the capillary number Ca and the ratio of dynamic viscosities of the two fluids $M = \mu_{nw}/\mu_w \sim 10^{-3}$ for the water/air system. The capillary number Ca, which is the ratio between viscous forces acting at the pore scale in water and capillary forces, is expressed as

$$Ca = \frac{\mu_{nw} Q_l}{A\gamma \cos\theta_w} \tag{1}$$

where γ is the surface tension, μ_{nw} is the liquid water dynamic viscosity, θ_w is the contact angle taken in the wetting fluid (air), A is the cross-sectional area of the sample (area of injected face) and Q_l is the injected flow rate.

To estimate Ca in the case of PEMFCs, we assume that all the water produced within the CL invades the GDL. This leads to express Ca as

$$Ca = \frac{\mu_{nw} i M_{H_2O}}{\gamma \cos\theta_w 2F\rho_l} \tag{2}$$

where F is the Faraday's constant, M_{H_2O} is the water molecular weight, ρ_l is the liquid water density and i is the current density. With $i = 1\,A\,cm^{-2}$ and $\theta_w = 70°$, Eq. (2) leads to $Ca \sim 10^{-7}$–10^{-8}. According to Ref. [18], the displacement for such low values of the capillary number is dominated by capillary effects and leads to a regime called capillary fingering. In this low capillary number limit, the drainage process can be simulated using the invasion percolation (IP) algorithm [19], at least when the contact angle θ_w is sufficiently low (see Section 3).

In the rest of this section we show how this algorithm can be implemented taking as an example the invasion within a 2D model fibrous medium.

2.1. Model fibrous medium and associated pore-network model

As depicted in Fig. 3, the system under consideration is formed by an array of equal-sized non-overlapping cylinders (disks) randomly distributed. This is similar to a cross-section through an anisotropic arrangement of equal diameter fibres. The disk configuration is generated using the Metropolis algorithm as described in Ref. [20].

The next step is to map the pore space onto a discretized interconnected network of sites (pores) connected by bonds (throats). To this end, we begin with the computation of the Voronoi diagram, following [20]. This leads to a partition of the domain into regions limited by polygons, as shown in Fig. 3. Each polygon

surrounds a disk so that each point inside the polygon is closer to this disk than to any other disk in the system. A segment of a Voronoi polygon is formed by points that are at the same distance from two disks. The polygon segments and polygon segments intersections are identified as the bonds and sites (pores) of the pore network, respectively. The size of a bond is identified as the diameter of the smallest circle with center on the bond and in contact with the two disks adjoint to the polygon segment forming the bond. In other terms, if C_1 and C_2 are the centers of the two disks adjoining the bond, the bond size ℓ is expressed as $\ell = |C_1C_2| - D$, where $|C_1C_2|$ and D are the Euclidian distance and disk diameter, respectively. For simplicity, no volume is associated with bonds, which act only as capillary barriers, as will be seen below. Volumes are associated with pores and correspond to the regions of pore space limited by the bond minimum apertures.

2.2. Drainage algorithm

As in any bond invasion percolation model on a network, the first step is to assign an invasion capillary threshold to each bond. In our case, the threshold is associated with the aperture minimum between the two disks limiting the bond. According to Laplace's law, the threshold capillary pressure reads

$$P_{\text{th}} = 2\gamma \cos\theta_{\text{w}} \left(\frac{1}{\ell} + \frac{1}{e} \right) \tag{3}$$

where e is the length of the cylinders. Note that the simulations are performed in 2D (which corresponds to $e = \infty$) whereas the experiment (see below) is carried out with finite equal length cylinders with $e > \ell$. Since $e > \ell$ and e is uniform, the capillary pressure threshold is essentially controlled by the minimum gap ℓ between the cylinders also in the experiments. Hence, we can use the approximation $P_{\text{th}} \approx (2\gamma \cos\theta_{\text{w}})/\ell$ both in the simulation and to interpret the experiment.

Implementing the IP algorithm is now straightforward. Initially, all bonds are occupied by the wetting fluid (air). The non-wetting fluid invades the network from one of its four sides; the bottom side in our case as depicted in Fig. 3. The algorithm then consists of repeating two steps:

1. Identify the bond adjacent to the invaded region that has the lowest invasion threshold.
2. Invade the identified bond and fill the adjacent pore up to the next cylinder minimum gaps.

With the two additional rules:

(3) Bonds not belonging to the percolation cluster skeleton cannot be invaded.
(4) Bonds belonging to trapped wetting fluid bond cluster cannot be invaded.

The percolation cluster refers to the set of bonds occupied by the defender (wetting) phase and connected to the exit side through at least one path of defender occupied bonds and pores.

The invasion stops when the non-wetting fluid forms a spanning cluster from bottom to topsides. No flow boundary conditions are imposed on lateral sides of network to fit in with the experimental conditions. The percolation cluster is identified using a depth search algorithm, e.g. Ref. [21].

Results of drainage simulation based on this algorithm are compared to experimental visualisations in a machined micromodel after the next section, which describes the experiments.

2.3. Experiments

A numerically generated hydrophobic model fibrous medium has been constructed using a digitally controlled milling machine. The fabrication procedure can be summarized as follows, see Ref. [22] for more details. First, 1 mm diameter, 1 mm long cylindrical holes are drilled into a Plexiglas plate with a micromiller. The machining precision is equal to 10 μm in every $(x; y; z)$ direction. The position of cylinders is generated numerically using the Metropolis algorithm as for the numerical model. More precisely, the same distribution of cylinders is used both in the experiment and the simulation. Note that the micromodel 1-mm depth is lower than the capillary length (which is on the order of 1.5 mm) in order to avoid gravity effects on the liquid distribution within the depth. Thus, apart from the uncertainties introduced in the course of fabrication, the pore space geometry in the model plane is the same in the experiment and the simulation. Then the plate is machined so as to contain the negatives of fluid supply and exit channels along the cylinders domain. The next step is to mould the machined Plexiglas plate with Rhodorsil® RTV-2 (a silicone elastomer). This gives a RTV slice containing the array of solid cylinders with the supply and exit channels. Then the RTV slice is sandwiched between a metallic support plate and a Plexiglas transparent cover plate. Tightness is obtained by compressing a little the RTV between the metallic and Plexiglas plates thanks to a series of equally spaced and controlled clamping screws. The exit channel along the topside of the cylinder array is open to ambient pressure, while the entrance channel along the bottom side is connected to a screw-driven pump. The micromodel is initially fully saturated with air and put on a horizontal table so as to avoid the influence of gravity effects.

Experiments are carried out by slowly injecting water into the micromodel from the bottom side. A constant temperature of 22 °C is maintained during the experiment. The experiment is recorded with a CCD camera set above the micromodel. There are some unavoidable experimental uncertainties concerning the exact reproduction of the numerical array of cylinder coming from the machining precision, elastic deformations of the materials, the plate's parallelism, etc. However, as we shall see, this does not prevent a favourable comparison between the experimental and numerical results.

The results reported in this paper have been obtained for a 2.5 cm × 2.5 cm model containing about 23 × 23 cylinders, as shown in Fig. 4. Note that the contact angle, taken in the water phase, is ≈110° for RTV/water/air [23], which is comparable to the value over teflonized surfaces. Thus, $\theta_{\text{w}} \approx 70°$. The water injection flow rate imposed in the experiment is 0.75 ml h^{-1},

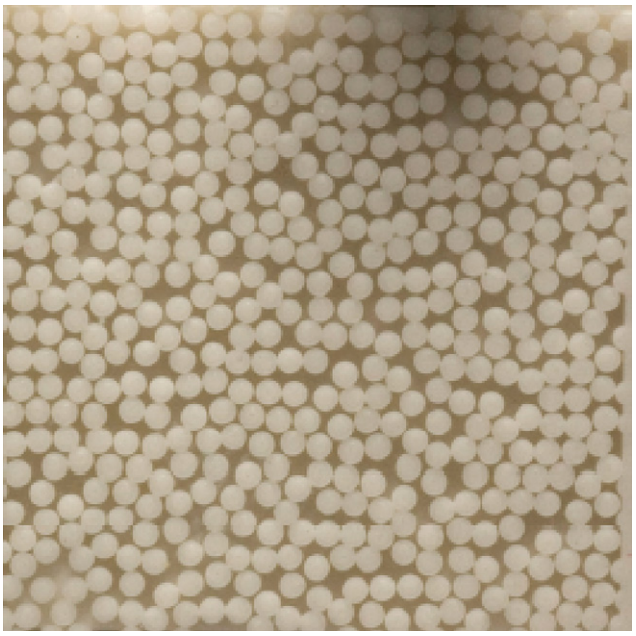

Fig. 4. Top view of physical micromodel.

which leads to $Ca \approx 5 \times 10^{-7}$. It can be noticed that the pore sizes in the experiments are larger than in a GDL material. However, this has no effect on the pattern provided that the capillary number is sufficiently small.

2.4. Invasion patterns

As mentioned before, the drainage simulation has been performed using the IP algorithm described in Section 2.2 over an array of disks in principle identical to the experimental model described in Section 2.3.

Fig. 5a shows the experimental invasion patterns obtained at different times in the physical model. Fig. 5b shows the numerical prediction using the IP algorithm on the network constructed from the Voronoi diagram at comparable saturations. Overall, the comparison in Fig. 3 shows a good agreement between the experimental observations and the numerical computations. Although the comparison could seem to be qualitative only, it should be pointed out that direct comparison between experimental and numerical results for the same microstructure are scarce in the literature. Often, the comparison is performed only between systems having the same statistical properties (porosity, pore and bond size distributions, average coordinance, etc.). Thus, it is interesting to see that the IP algorithm leads to good results on a particular realisation, which is as much as possible identical to the experiment.

Some differences can be observed, however, for example at the beginning of the drainage process or at breakthrough (Fig. 5). These differences could be attributed to the previously mentioned uncertainties induced by the micromodel fabrication or to viscous effects. The viscous effects are neglected in the simulations. Although the experiment is conducted at a very low capillary number, a slight influence of viscous effects could affect the invasion patterns compared to the purely quasi-static ones obtained in the simulation, see Ref. [18]. A possible source of discrepancy may be found in the relatively high contact angle characterizing the experimental system. This issue is explored in detail in the next section.

Before, we note that the capillary fingering regime illustrated here is qualitatively consistent with the liquid clusters that have been observed in a GDL by means of synchrotron X-ray radiographies [13]. The invasion patterns reported in Ref. [14] also resemble IP patterns. However, as pointed out in Ref. [15], the injected flow rate considered in Ref. [14], is about two orders of magnitude greater than the flow rate expected in an operating fluid cells, which leads to a capillary number of the order of 10^{-6}–10^{-5}. Hence the invasion process considered in Ref. [14] is likely to be affected by viscous effects.

3. Impact of wettability on the invasion pattern

An important issue in relation with the crucial problem of water management in PEMFCs is the influence of wettability conditions on invasion pattern. Since the capillary number characterizing the water invasion in GDLs is expected to be very small, we consider capillarity-dominated regimes only (no viscous effects). In this quasi-static limit, we investigate the influence of contact angle on the invasion pattern, considering again a 2D model fibrous medium.

To facilitate the numerics, this model is slightly different from the one considered in the previous section. As depicted in Fig. 6, disks (the solid phase of the fibrous medium) are placed on a square lattice of constant lattice spacing a. Disks radii are randomly distributed according to a uniform distribution law in the range $[R_{\min}, R_{\max}]$. For the simulations presented in the following, we considered an array of 14×20 disks with $R_{\min} = R_{\max}/3$ and $R_{\max} = 0.48a$. This model is similar to the ones considered in Ref. [24] but adapted for flow rate controlled invasion rather than pressure-controlled invasion.

The interface between the invading and displaced fluids consists of a sequence of arcs between pairs of disks (in Fig. 6, which shows the invading fluid at the entrance of the system before the first invasion, the invading fluid is in grey, the displaced fluid is in white and the interface is visible as a series of arcs joining the bottom row of disks). At each step of the invasion, one "interfacial pore" of the system is invaded. A "pore" is defined as the region of the pore space located inside the square formed by the segments joining two neighbour disks on the square lattice. An interfacial pore is a pore not yet invaded containing at least one arc. Interfacial pores are indicated with a "A" in Fig. 6. To determine which interfacial pore should be invaded at a given step of the invasion, we determine the "critical" invasion curvature radius of each interfacial arc. As sketched in Fig. 7, this consists in studying the arc curvature radius as the arc moves between the two disks it intercepts. As discussed in Ref. [24], there are three main local growth mechanisms controlling the invasion. The first, as illustrated in Fig. 7a, is called "burst". It corresponds to the burst of the meniscus when the local capillary pressure exceeds the maximum local capillary pressure compatible with a stable arc joining the pair of disks under consideration, see Ref. [24] or [22] for more details. We

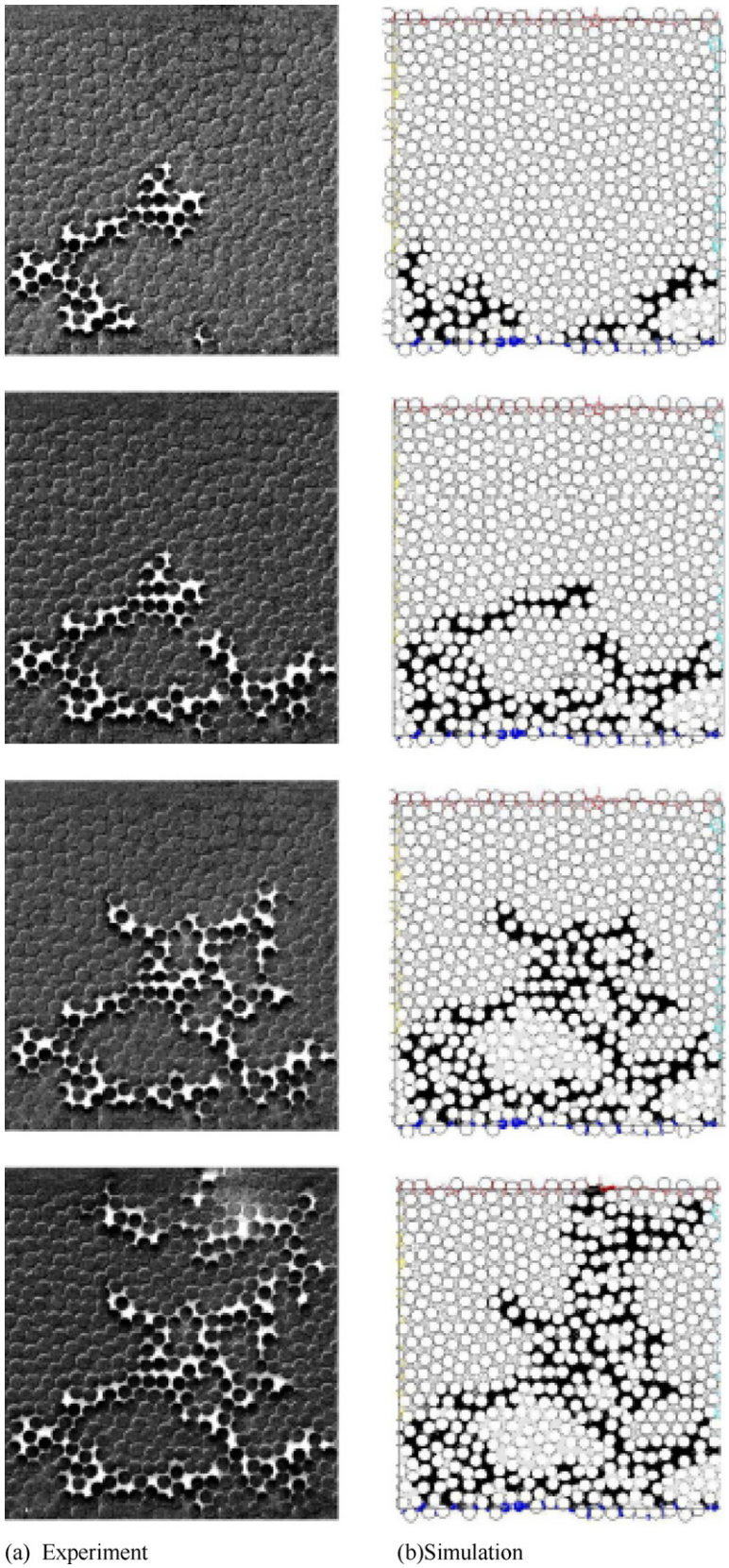

Fig. 5. (a) Displacement patterns observed during the slow drainage experiment within the model porous medium. Water (in white) injected from the bottom edge displaces air (in dark grey). (b) Simulated displacement patterns using the IP model on the Voronoi network. Invading phase in black.

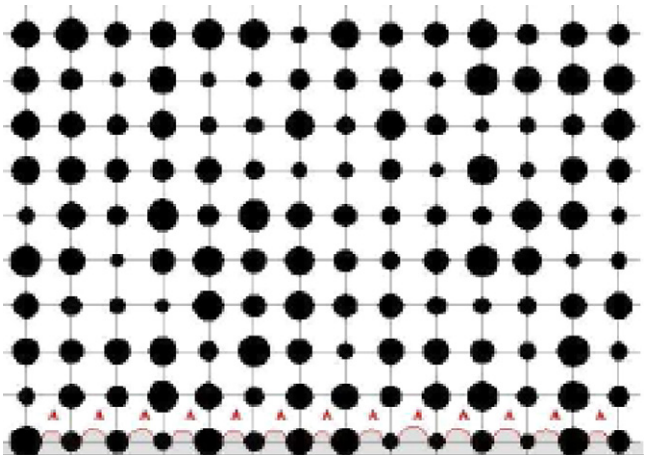

Fig. 6. Model fibrous medium formed by a regular array of disks of variable diameter (invading fluid in grey, displaced fluid in white). The interface is visible as a series of arcs joining the bottom row of disks.

note r_b the arc curvature radius corresponding to the last arc stable before burst. As sketched in Fig. 7b–d, the local capillary pressure corresponding to the arc burst may be not reached because another event occurs before: the considered arc touches a third disk during its growth, Fig. 7b, or coalesces with another arc, Fig. 7c and d. If this happens, we compute the arc radius of curvature corresponding to each of these local events with r_t the radius corresponding to the touch event and r_c the radius corresponding to the coalescence event, if any. These radii are computed as functions of contact angle, disks radii and distances between disks [24,22]. We affect to each interfacial arc the radius $r_a = \max(r_b, r_t, r_c)$. This gives a hierarchy of radii. At each step of the invasion, the interfacial pore associated with the arc(s) corresponding to max (r_a), i.e. the minimum invasion threshold local capillary pressure, is invaded. The corresponding "unstable" arc(s) is (are) suppressed from the list of interfacial arcs and new arcs are created at the periphery of the invaded pore. This procedure is repeated until breakthrough. Again the interested reader can refer to [22] or [24] for more details on the invasion procedure.

Fig. 8 shows the evolution of the invasion pattern as a function of the contact angle θ_E (contact angle taken in the displaced fluid). If liquid water is supposed to be the invading fluid, a hydrophobic fibrous medium corresponds to $0 \leq \theta_E < 90^\circ$, whereas a hydrophilic one corresponds to $90^\circ < \theta_E \leq 180^\circ$. As can be seen from Fig. 8, the wettability has a major impact on the invasion pattern. For the low contact angles (⇔very hydropho-

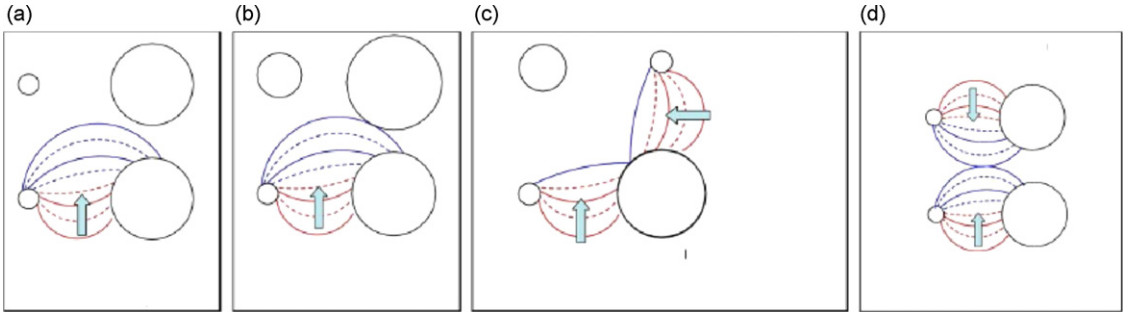

Fig. 7. Growth of interfacial arcs during the invasion. The arrows indicate the meniscus displacement direction. Local invasion events: (a) burst, (b) touch, and (c) and (d) arc coalescence.

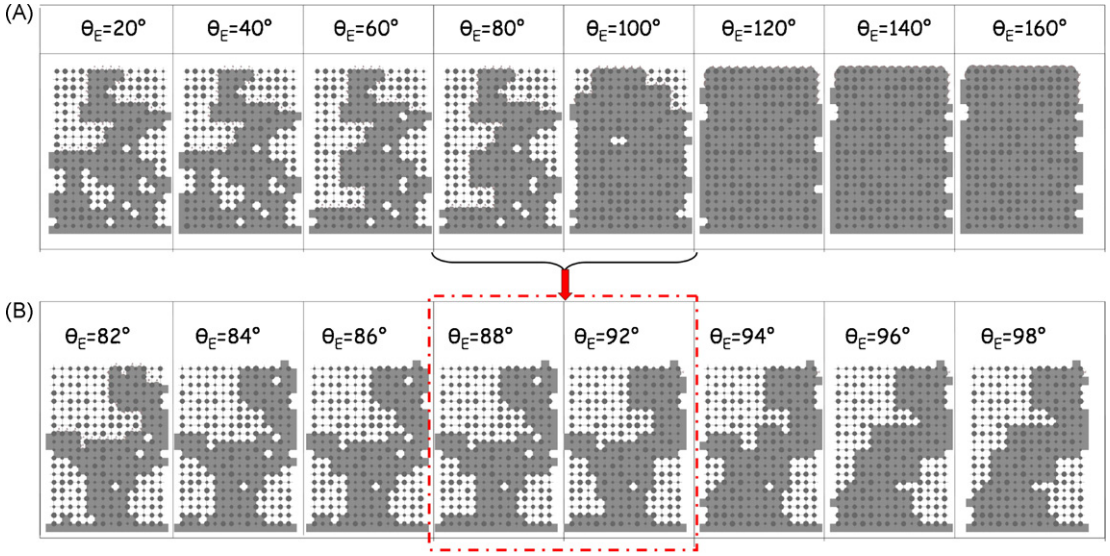

Fig. 8. (A) Evolution of invasion pattern at breakthrough in a model fibrous medium as a function of contact angle in the displaced fluid θ_E. Invading phase in grey, displaced phase in white. (B) Detailed evolution of the pattern in the range of contact angles [82°, 98°].

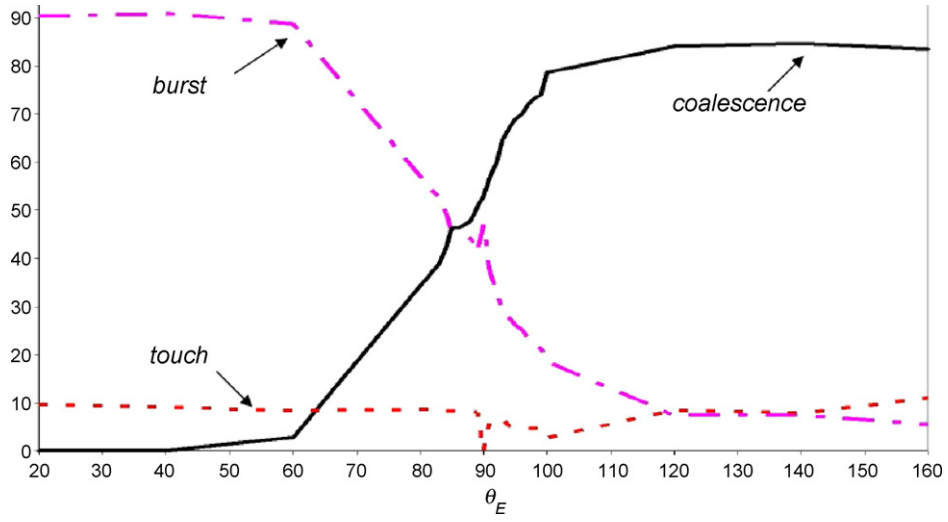

Fig. 9. Probability (in %) of interface local growth mechanisms as a function of contact angle in the displaced fluid.

bic GDL), capillary fingering is obtained as in Section 2. For contact angles greater than about 100° (⇔hydrophilic GDL), a compact pattern characterized by an almost flat invasion front is obtained. It is interesting to mention that the transition between the two patterns is not abrupt at 90° but mainly occurs in the range of contact angles [80°, 100°].

The change in the invasion pattern can be explained by the change in the interface local growth mechanisms. We have plotted in Fig. 9 the probability of each elementary local growth mechanisms as a function of contact angle (for the single realisation of the medium considered here, the probability of a given elementary event is simply n_e/n_p where n_e is the number of pores invaded as a result of the considered local event/mechanism and n_p is the number of pore invasion to reach breakthrough).

As can be seen from Fig. 9, burst is the dominant mechanism for low contact angle, and the invasion can be simulated using the IP algorithm as in Section 2. For contact angles greater than about 100°, coalescence of menisci is the dominant mechanism and the invasion can be simulated very simply by a flat travelling front (note however that for sufficiently high contact angles above 100°, film effects can complicate the invasion with certain pore geometries, e.g. Ref. [25] and references therein).

On the basis of the results shown in Figs. 8 and 9, the slight differences observed between the experiment and the simulation in Section 2 can be attributed to the fact that the local displacement in the experiment is not completely dominated by the burst mechanism (as opposed to the simulation in Section 2 where only the burst mechanism is taken into account) since the contact angle in the experiment is relatively large ($\theta_E \sim 70°$).

4. Impact of wettability on evaporation pattern

Suppose that the GDL is completely saturated by water after flooding. One obvious option to restore the GDL is to circulate a dry gas within the bipolar channel so as to dry out the GDL. We wish to explore the impact of wettability on drying pattern and drying time. To this end, we again consider 2D model porous media and perform drying experiments with two physical models of same microstructure but of different wettability. One is machined in a PTFE plate and is hydrophobic. The second is machined in a Plexiglas plate and is hydrophilic ($\theta_{water} \sim 80°$). A 1-cm thick flat Plexiglas plate is fixed on top of the machined plate. This transparent plate allows for the direct visualisation of evaporation pattern. For the hydrophobic system, a very thin silicon oil film carpets the top Plexiglas plate so as to make it hydrophobic (with a static contact angle close to 110°).

In continuity with previous studies on drying of network micromodels, we do not adopt a disk array structure as before, but rather a square geometry like in Ref. [26]. This does not affect, however, the findings reported in this section. The microstructure of the machined models is shown in Fig. 10. Note that the 1-mm depth of machined ducts is uniform, lower than the capillary length and greater than the duct widths, so that the invasion is essentially controlled by the duct width and not by its depth. The channel width is distributed randomly according

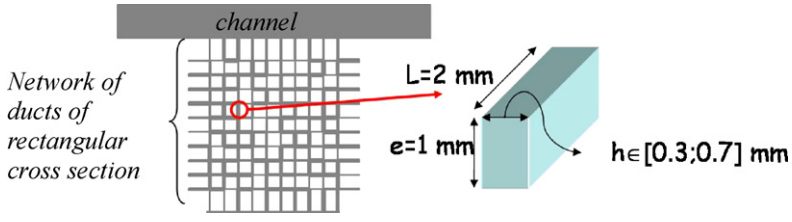

Fig. 10. Model porous medium used for the evaporation experiment.

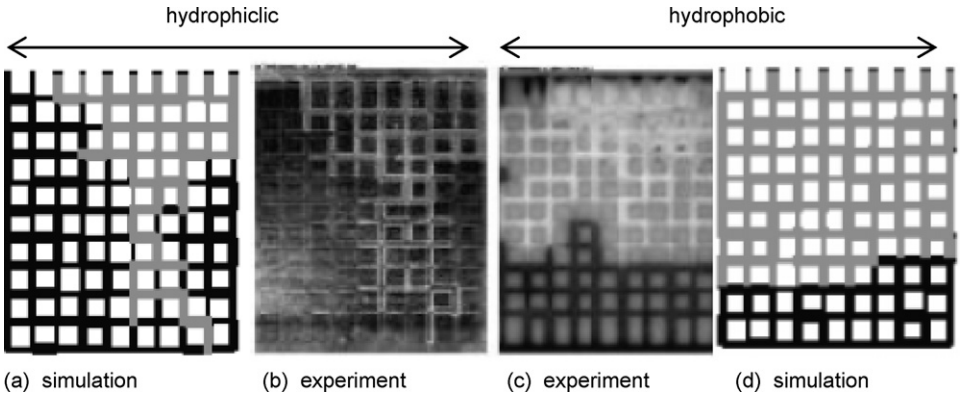

Fig. 11. Evaporation patterns (gas phase in grey or white (c), water in black or dark grey, the little rectangles of random size form the solid matrix). (a) Simulation of evaporation in the hydrophilic network, (b) experimental pattern in hydrophilic network, (c) experimental pattern in hydrophobic network, and (d) simulation of evaporation in the hydrophobic network.

to a discrete uniform distribution. Except for the uncertainties associated with the machining process, five classes of channel width are considered: 0.3, 0.4, 0.5, 0.6 and 0.7 mm. A 5 mm in width, 3 mm in depth and 45 mm long channel is machined along the top edge of the network as shown in Fig. 10.

The network is initially filled with distilled water. Evaporation is driven by the flow of air at controlled relative humidity in the channel. The relative humidity (RH) is controlled by circulating the air in a chamber containing a LiCl solution (RH = 12%). The system, including the network and the channel, is placed in a chamber of controlled temperature (40 °C). The experiments are recorded with a CCD camera set above the chamber.

The obtained evaporation patterns are shown in Fig. 11. As can be seen from Fig. 11b, the evaporation pattern in the hydrophilic model resembles a capillary fingering pattern. This result was expected. From previous studies, e.g. Ref. [27] and references therein, it is known that slow evaporation and quasi-static drainage lead to the same invasion pattern except for the isolated clusters that are trapped for good in drainage but not in the evaporation situation since they are subject to evaporation. Fig. 11a shows the pattern obtained with the pore-network evaporation model proposed in Ref. [28]. As described in Ref. [29], this model combines the invasion percolation algorithm with the computation of diffusion transport of the water vapour in the

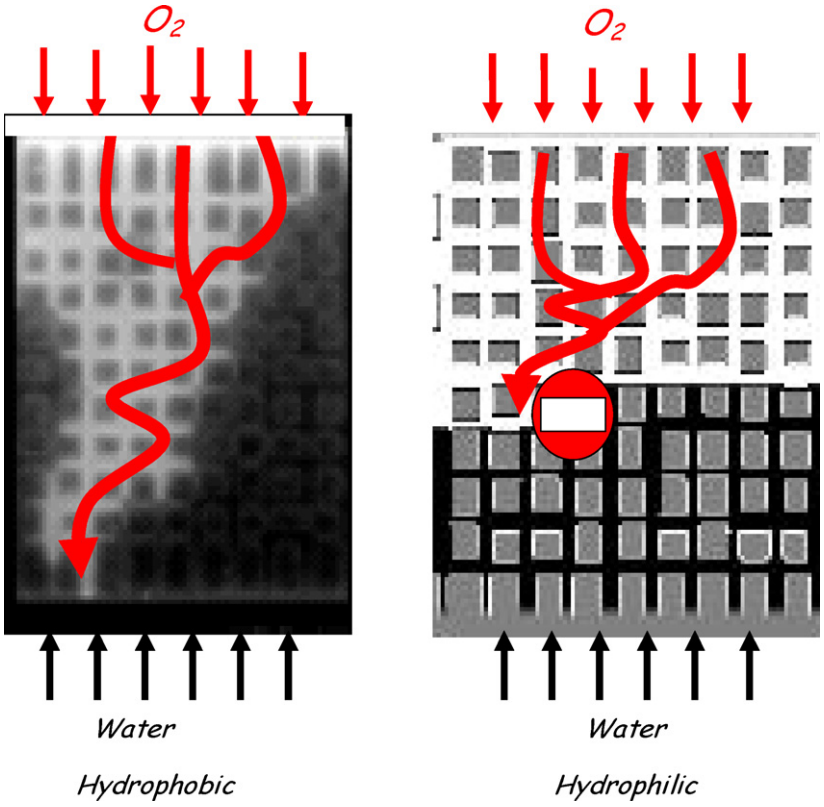

Fig. 12. Sketch of liquid invasion and O_2 transport in a hydrophilic GDL and a hydrophobic one.

gas phase. As can be seen from Fig. 11a and b, the agreement is good between the experimental and the simulated patterns. As previously, the slight differences between the two patterns are attributed to the effect of contact angle, which is on the order of 80° in the experiment. Again, from Section 3, we know that, contrary to what it is assumed in the simulation, the invasion is not controlled only by the burst mechanism for such a high value of contact angle (see Figs. 8 and 9).

Evaporation in the hydrophobic model, see Fig. 11c, leads to a compact pattern with an almost flat invasion front reminiscent of the pattern obtained numerically for $\theta_E > 100°$ in Section 3, see Fig. 8. For the hydrophobic network, air is the wetting fluid and liquid water is the non-wetting one. Hence slow evaporation in this case is analogous to the process of displacement of a non-wetting fluid by a wetting one. This process is usually called imbibition, e.g. Ref. [11]. It is therefore not surprising that evaporation leads in this case to an imbibition pattern. As illustrated in Fig. 11d, it is possible to develop pore-network simulation of evaporation in the hydrophobic network by combining local imbibition rules and the computation of the diffusion transport in the gas phase, see Ref. [29].

The great difference in the patterns between the hydrophobic and the hydrophilic networks are associated with differences in drying time (for the same condition in the channel). This was explored in detail in Ref. [29], where it is shown that drying is faster in the hydrophilic network. In square networks, drying can be about up to 46% faster in small 10×10 hydrophilic networks compared to a hydrophobic one of the same size. The discrepancy in drying time decreases, however, with the network size, with drying about 25% faster in a hydrophilic network for large networks.

5. Discussion and conclusion

As regards two-phase flows and evaporation in GDLs, the main outcomes of the results presented in this paper can be expressed as follows:

- Rendering the GDL hydrophobic is a good option. As sketched in Fig. 12, large regions of the pore space remains accessible to the gas phase up to the CL/GDL interface in the capillary fingering regime that characterizes water invasion in a hydrophobic GDL. In contrast, the compact invasion in a hydrophilic GDL is very detrimental to the gas access to the GDL/CA interface. As a result, the liquid saturation S at breakthrough (when the liquid reaches the channel) in the hydrophobic GDL is much lower than for a hydrophilic one (where $S_{BT} \sim 1$). Thus our results provide a pore-scale physical explanation to the fact that it is advantageous to use hydrophobic GDLs.
- Drying is faster with a hydrophilic GDL. However, the difference in drying time with a hydrophobic GDL is not sufficient to counterbalance the advantages of a hydrophobic GDL in terms of liquid distribution during the GDL invasion by water.
- The capillary number characterizing the liquid flow in a GDL is very small. Combined with the fact that a GDL is a very thin system, the flow can then be considered as dominated by capillary effects. To simulate the liquid flow in this quasi-static regime in a hydrophobic GDL at the scale of the microstructure, one can rely on the IP algorithm as a first approximation. However, as shown in Section 3, the local invasion mechanisms are not dominated by the burst mechanism for "large" contact angles θ_E approaching 90°. This leads to changes in the invasion pattern compared to the IP pattern. We recall that $\theta_E \sim 70°$ for the air/water/PTFE system and even closer to 90° within a GDL material according to [9]. This should be kept in mind when comparing experimental data and simulations based on the IP algorithm (or the algorithm used for example in Ref. [15], which is equivalent to IP).
- The fact that the invasion regime (compact vs. capillary fingering) is completely different depending on the wettability of the GDL suggests that it is not correct to use basically the same Leverett function and the same expressions of relative permeabilities whatever the wettability of the GDL, e.g. Ref. [16].

In our study, only 2D systems have been considered. It is naturally desirable to consider 3D systems, e.g. Refs. [13,15]. This makes significantly more difficult the numerical simulations and the visualisations. The 2D results presented here may serve as guidelines in the analysis of 3D results. In particular, all the results listed above are expected to be qualitatively valid in 3D.

Since a MPL is often attached to the GDL, it is interesting to study two-phase flows in MPL. Using multi-scale pore networks would be interesting in this perspective. In the same spirit, pore-network simulations would be certainly useful to understand better the complex interactions between the electrochemical and transport phenomena, including two-phase flows and wettability effects, in catalyst layers as well as the interactions between the various layers forming a PEMFC.

Acknowledgements

Financial supports from 5th PCRD European Program FEBUSS and GIP ANR (project ANR-06-PANH-022-02 "Chameau") are gratefully acknowledged.

References

[1] T. Berning, D.M. Lu, N. Djilali, J. Power Sources 106 (2003) 284–294.
[2] H. Meng, C.Y. Wang, Chem. Eng. Sci. 59 (2004) 3331–3343.
[3] K.W. Lum, J.J. McGuirk, J. Power Sources 143 (1/2) (2005) 103–124.
[4] A.Z. Weber, J. Newman, Chem. Rev. 104 (2004) 4679–4726.
[5] N. Djilali, Energy 32 (2007) 269–280.
[6] F. Barbir, PEM Fuel Cells: Theory and Practice, Elsevier Academic Press, 2005.
[7] C.Y. Wang, in: W. Vielstich, H.A. Gasteiger, A. Lamm (Eds.), Two-phase Flow and Transport in Handbook of Fuel Cells—Fundamentals, Technology and Applications, John Wiley & Sons, 2003 (Chapter 29).
[8] H. Tavana, A.W. Neumann, Colloids Surf. A: Physicochem. Eng. Aspects 282/283 (2006) 256–262.
[9] V. Gurau, M.J. Bluemle, E.S. De Castro, Y.-M. Tsou, J.A. Mann Jr., T.A. Zawodzinski Jr., J. Power Sources 160 (2006) 1156–1162.
[10] V. Gurau, J.A. Mann, T.A. Zawodzinski, ECS Transactions 3 (1) (2006) 1095–1104.

[11] F.A.L. Dullien, Porous Media. Fluid Transport and Pore Structure, Academic Press, 1991.
[12] J. Bear, Y. Bachmat, Introduction to Modeling of Transport Phenomena in Porous Media, Kluwer Academic Publishers, Dordrecht, The Netherlands, 1990.
[13] I. Manke, C. Hartnig, M. Grunerbel, W. Lehnert, N. Kardjilov, A. Haibel, A. Hilger, J. Banhart, H. Riesemeier, Appl. Phys. Lett. 90 (2007) 174105.
[14] S. Litster, D. Sinton, N. Djilali, J. Power Sources 154 (2006) 95–105.
[15] V.P. Schulz, J. Becker, A. Wiegmann, P.P. Mukherjee, C.Y. Wang, J. Electrochem. Soc. 144 (4) (2007) B419–B426.
[16] J.H. Nam, M. Kaviany, Int. J. Heat Mass Transfer 46 (2003) 4595–4611.
[17] U. Pasaogullari, C.Y. Wang, J. Electrochim. Soc. 151 (2004) A399–A406.
[18] R. Lenormand, E. Touboul, C. Zarcone, J. Fluid Mech. 189 (1988) 165–187.
[19] D. Wilkinson, J.F. Willemsen, J. Phys. A: Math. Gen. 16 (1983) 3365–3376.
[20] S. Torquato, Random Heterogeneous Materials, Microstructure and Macroscopic Properties, Springer, 2002.
[21] F. Babalievsky, Int. J. Mod. Phys. C 9 (1) (1998) 43–60.
[22] O. Chapuis, Influence des conditions de mouillage sur les déplacements quasi-statiques eau-air et l'évaporation en milieux poreux modèles. Application à la gestion de l'eau dans les piles à combustibles de type PEMFC, Thèse INPT, 2006.
[23] N. Sghaier, M. Prat, S. Ben Nasrallah, Chem. Eng. J. 122 (2006) 47–53.
[24] M. Cieplak, M.O. Robbins, Phys. Rev. B 41 (1990) 508–521.
[25] M.J. Blunt, H. Scher, Phys. Rev. E 52 (6) (1995) 6387–6403.
[26] M. Prat, Int. J. Heat Mass Transfer 50 (2007) 1455–1468.
[27] M. Prat, Chem. Eng. J. 86 (1/2) (2002) 153–164.
[28] M. Prat, Int. J. Multiphase Flow 19 (4) (1993) 691–704.
[29] O. Chapuis, M. Prat, Phys. Rev. E 75 (2007) 1–11 (046311).